Available online at www.sciencedirect.com
ScienceDirect
International Journal of Multiphase Flow 33 (2007) 525–544
International Journal of Multiphase Flow
www.elsevier.com/locate/ijmulflow

Spray impact onto flat and rigid walls: Empirical characterization and modelling

Davood Kalantari *, Cameron Tropea

Chair of Fluid Mechanics and Aerodynamics, Darmstadt University of Technology, 64287 Darmstadt, Germany

Received 26 February 2006; received in revised form 20 September 2006

Abstract

An experimental study of spray impact onto horizontal flat and rigid surfaces is presented and used as input data for a new empirical model. A phase Doppler instrument has been used to measure drop size and two components of velocity directly above the target. The average film thickness formed due to spray impact has been measured using a high-speed CCD camera. The spray–wall interaction has been characterized in terms of correlations for the velocity and trajectory of secondary droplets and the mass and number ratio of the secondary spray. The novel aspect of the model is that the correlations are based on mean statistics over many events and not on the outcome of single drop impact experiments. Furthermore a rather large range of oblique impact angles have been studied and incorporated into the empirical models as an influencing factor.

Keywords: Spray; Spray impact; Secondary spray; Liquid film

1. Introduction

Spray impingement onto walls occurs in many industrial and technical applications, such as direct injection in Diesel engines, gas turbines, agricultural sprays, spray cooling, spray painting and spray coating. Physically two important interacting hydrodynamic phenomena must be correctly captured in describing spray impact: the generation of secondary droplets and the liquid film accumulating on the wall, the latter aspect often being neglected in spray impact models. However, prediction of average film thickness and average velocity is very important in the case of spray cooling systems or for fuel injection sprays onto heated walls because these parameters significantly affect the efficiency of heat transfer in the sprayed surfaces. Also the average film thickness can affect the properties of secondary spray, splashing threshold, ejected mass and number of secondary droplets. In some applications, it is desirable to eliminate the deposited film on the wall as far as possible, e.g. in internal combustion engines, whereas m some cases the maximum deposition is required,

* Corresponding author. Tel.: +49 6151 16 3654; fax: +49 6151 16 4754.
E-mail address: d.kalantari@sla.tu-darmstadt.de (D. Kalantari).

0301-9322/$ - see front matter © 2006 Elsevier Ltd. All rights reserved.
doi:10.1016/j.ijmultiphaseflow.2006.09.008

e.g. in spray coating, spray painting or agricultural sprayers. On the other hand, the induced fluctuations in liquid layer formed on the rigid walls may decrease the quality of coated or painted surfaces.

Much of the previous literature on the topic of spray impact experimentally addresses deposition, usually being restricted to the normal impact of single droplets onto a solid dry or wetted wall or sometimes onto a thin liquid film, where generally the impact conditions can be carefully controlled, see e.g. (Bai and Gosman, 1995; Bai et al., 2002; Mundo et al., 1998; Stanton and Rutland, 1998), and such results serve as a basis for model formulations. Prevailing models extrapolate the results of single droplet impact to the case of a spray–wall interaction by simple superposition of many individual droplets. However such simplified models neglect to consider numerous effects regarding spray–wall interaction such as: the influence of the deposited film on the secondary spray, the tangential momentum of oblique impacting droplets that exist in the case of real spray impact conditions; effect of film fluctuations on the outcome of impacting droplets; effect of multiple droplet interactions and also the creation of the central jets and droplets due to break-up of the liquid film under impacting drops or to the interaction between uprising jets or crowns with impacting drops or other splashing droplets.

Our observations and that of other investigations, e.g. Sivakumar and Tropea (2002) indicate clearly that the splash created by a drop in a spray differs significantly from that of an isolated single drop impact or from the impact of a train of drops on a stationary liquid film, examined by Cossali et al. (1997) and Yarin and Weiss (1995). These differences can be easily seen in Fig. 1a and b, indicating that splash of a droplet in spray impact is much more irregular and non-symmetric in comparison to the symmetric propagation of a crown in the case of an isolated single droplet impact onto an undisturbed liquid layer.

One exemplary sketch of a non-symmetric splash in a spray is illustrated in Fig. 2. As shown in this sketch, one main source of this non-symmetric splash is the impact of a neighbouring droplet during the splash. If during the splash of a given droplet in a spray, other droplets impact close to the splashing droplet, then the higher hydrodynamic pressure exerted in the film near the base of the crown will feed fluid into the crown body on one side, yielding a non-symmetric splash. The thickness of the crown body and the crown height on this side will be larger than the other side, therefore secondary droplets ejected on this side will be larger due to the thicker rim bounding the crown, see Fig. 2. Similar behaviour can also b observed due to oblique impact of a droplet in spray. Such examples of asymmetry splashing can be seen in Fig. 1b.

In the case of spray impact, the non-dimensional crown height and radius do not exhibit a systematic dependence on the impact Weber number (Sivakumar and Tropea, 2002). This is in contrast with the result of an isolated single droplet impact on a stationary liquid film examined by Cossali et al. (1999). Observation of Sivakumar and Tropea (2002) indicates that in a spray impact the crown radius exhibits a growth rate

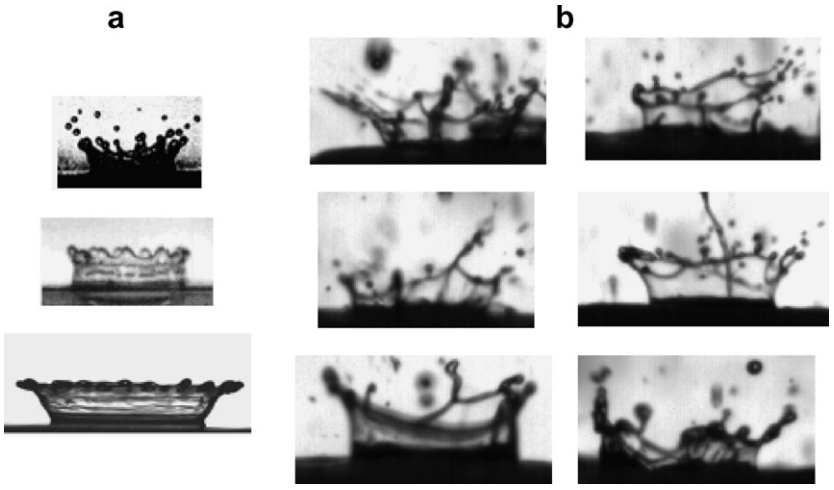

Fig. 1. Morphological comparison between splashes created by: (a) an isolated single drop, and (b) by a drop in a spray, time interval between frames is 62.5 μs.

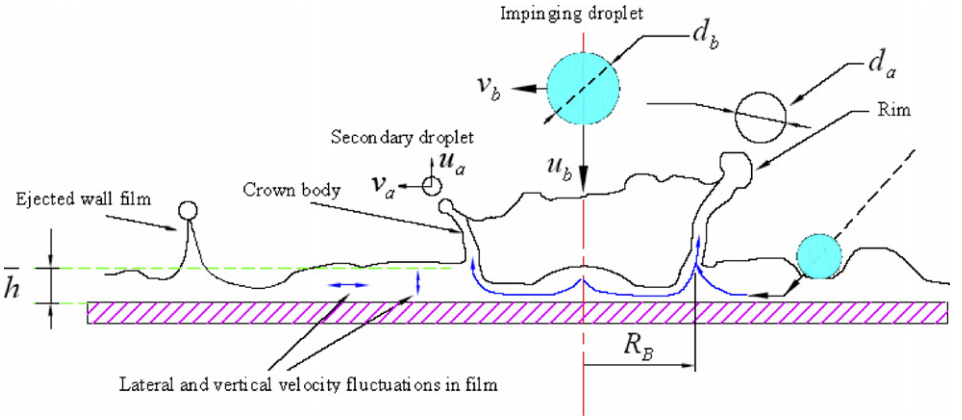

Fig. 2. Sketch of a splashing droplet in a spray, depicted as non-symmetric due to neighbouring drop impacts.

proportional to $t^{0.2}$, significantly different than that of a single or train of single droplets impacting onto an undisturbed liquid layer, $\sim t^{0.5}$, as investigated theoretically by Yarin and Weiss (1995). In both cases the maximum crown heights are comparable, whereas the maximum crown radius is much smaller in the case of splashing in a spray. Also the crown retraction is more rapid in a spray. The observations of Sivakumar and Tropea (2002) can be confirmed in the present study. An exemplary sequential photographic image of a splashing droplet in a spray is presented in Fig. 3. These sequential images were recorded by means of a high-speed camera with 16 kfps. In this picture a liquid droplet with impact Weber number of 534 splashes on a rigid surface in a dimension less accumulated film thickness of $\bar{h}/d_b = 0.57$, where $\bar{h}$ is the average film thickness and d_b is the diameter of the impacting droplet.

In Fig. 4a and b, the non-dimensional crown base radius ($R_B^* = R_B/d_b$) and crown height ($H_C^* = H_C/d_b$) are presented as a function of dimensionless time ($t^* = t \cdot u_b/d_b$) for the splashing droplet sequences illustrated in Fig. 3. In these pictures, non-dimensional crown base radius and height have a growth rate proportional to $(t^* - 0.1)^{0.3}$ and $(t^* - 0.5)^{0.28}$, respectively. These growth rates for the crown base radius and height for a splashing droplet in a spray are significantly different than that of a single or train of single droplets impacting onto an undisturbed liquid layer, proportional to $t^{0.5}$.

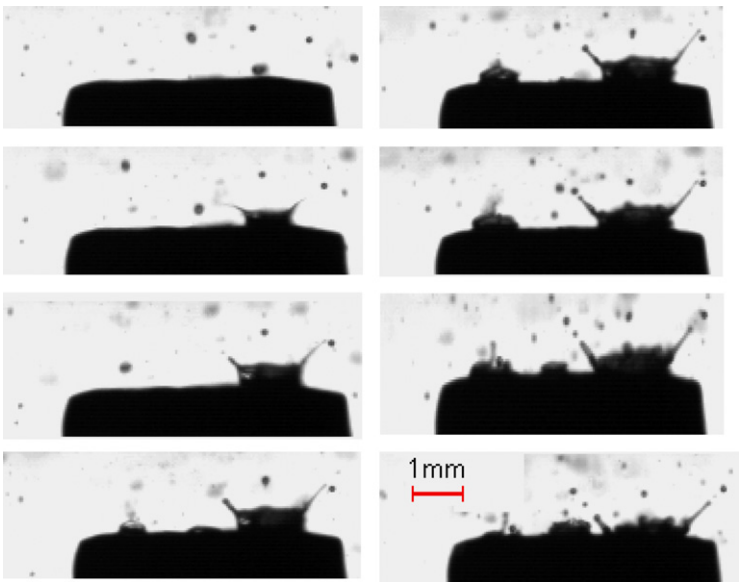

Fig. 3. Photographic image sequence of a splashing droplet in a spray. Recorded at 16 kfps; $We_{nb} = 534$ and $\bar{h}/d_b = 0.57$.

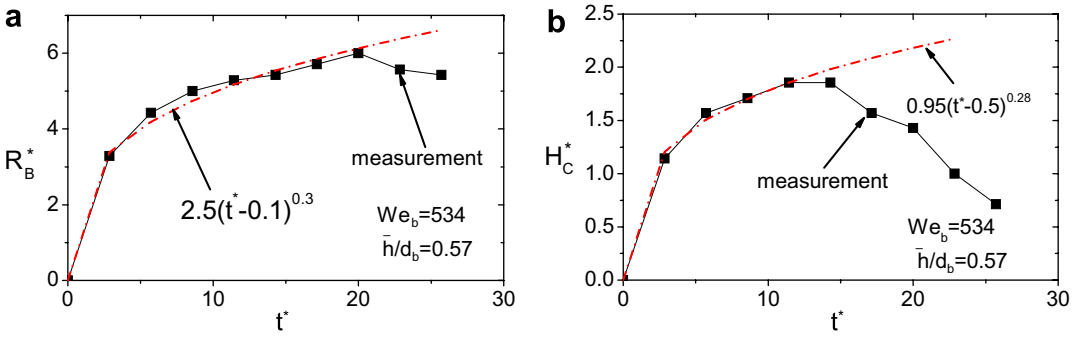

Fig. 4. Temporal variation of: (a) crown radius and (b) crown height of a drop splashing in a spray ($t^* = t \cdot u_b/d_b$, $We_{nb} = 534$ and $\bar{h}/d_b = 0.57$).

Based on the measurements conducted in this study, the non-dimensional crown base radius and crown height of a splashing droplet in a spray as a function of dimension less time con be expressed in the

$$R_B^* \sim (t^* - \tau_R)^{n_R} \quad 0.1 \leqslant \tau_R \leqslant 2.5 \quad \text{and} \quad 0.2 \leqslant n_R \leqslant 0.32 \tag{1}$$

$$H_C^* \sim (t^* - \tau_H)^{n_H} \quad 0.5 \leqslant \tau_H \leqslant 3.5 \quad \text{and} \quad 0.25 \leqslant n_H \leqslant 0.5 \tag{2}$$

where τ_R and τ_H are dimensionless constants obtained from the experimental data and are related to the initial conditions of the splash.

The difference of crown behaviour in a spray compared to single drop impacts has been examined by Roisman and Tropea (2004) in which the temporal expression of the crown has been described using a model for short-wave fluctuations in the liquid film. Agreement with the experimental observations of Sivakumar and Tropea (2002) is good.

While some of these effects have been previously investigated in isolation, see e.g. Roisman et al. (2002), the overall behaviour in a spray may involve a combination of effects. Therefore, data from impacting sprays and not just from single drop impacts are indispensable for formulating and verifying models. This is also the main purpose of the present work. The models in this study have been formulated on the basis of average quantifies of drops in a spray before and after impact (e.g. mean drop diameter, velocity and trajectory).

In general, spray impingement on walls is characterized by the generated secondary spray and the fluctuating liquid wall film. The thickness of the film varies from microns to millimeters, depending on the condition of impacting spray and the boundary conditions on the target.

Fig. 5 illustrates the origins of secondary droplets: from a splash with disintegrating crowns, from liquid jetting from the liquid film, or from rebounding droplets. Especially for inertial dominated dense sprays, multiple finger-like jets ejected from the film are observed and first analyses have been presented by Roisman and Tropea (2005) to estimate their frequency and size, see also Roisman et al. (2006).

Based on the previous studies, droplets can rebound for relatively low impact energy of the primary droplets. A droplet rebounds from the wall if the surface energy of the droplet at the end of partial spreading is larger than the kinetic and surface energy of the impacting droplet minus the viscous energy dissipation during the spreading. Threshold criteria is given by Bai and Gosman (1995) for "Rebound-deposition" as $We_{nb} = 5$ ($We_{nb} = \rho u^2 d/\sigma$; where u is the normal velocity component before impact, ρ is liquid density and σ is the surface tension) based on the result of an isolated single drop impact, or $We_{nb} = 20$ for spray impact conditions based on the observation of Lee and Hanratty (1988) and Ching et al. (1984). Also the observations of Wang and Watkins (1993) show that rebound occurs only for $We_{nb} < 30$. Drop rebound is also observed for oblique impacts, whereby the threshold criterion is generally considered still valid if only the normal component of velocity is used in computed the impact Weber number, Sikalo et al. (2005). Especially the effect of impact obliqueness will be considered in the present study. Indeed, the Weber number ratio (We_{tb}/We_{nb}) will be

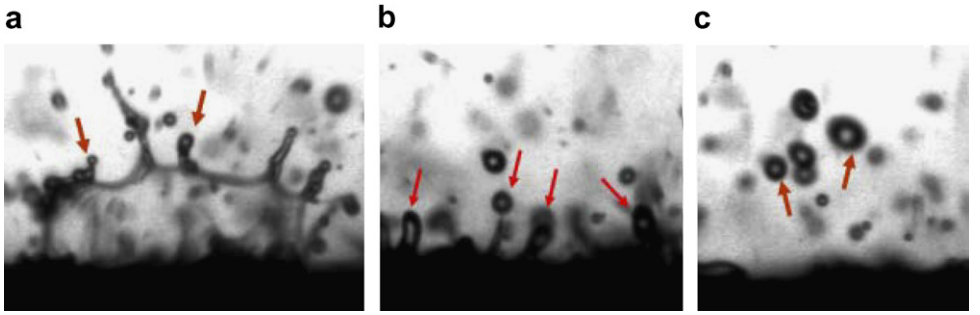

Fig. 5. Different sources for generation of secondary droplets and formation of liquid film on the wall, secondary droplet ejected from: (a) splashing droplet; (b) ejected wall film; (c) rebounded droplet.

shown to be a convenient parameter in which to base a threshold for rebounding ($We_{tb} = \rho v^2 d/\sigma$, where v is the tangential velocity component before impact). An exemplary sequence of a rebound in a spray impact phenomena is illustrated if Fig. 6. In this picture, the impact Weber number based on the normal velocity component is 10; the impinging angle is 58° and the diameter of the impinging droplet does not change throughout the impact, i.e., $d_b \cong d_a$ (b: before, a: after impact).

Splashing occurs at higher values of the normal impact Weber number, $We_{nb} > 80$ and it appears that the tangential velocity component does not play any important role in the onset of splashing. Observation of Coghe et al. (1999) shows that each splashing drop generates at least 10 tiny droplets. Physically break-up of a droplet occurs in the final stage of spreading in which the jetting lamella becomes unstable and generates a cloud of very small droplets. This occurs when the total energy of a droplet at the final stage of spreading is larger than its surface energy.

The overall structure of the accumulated wall film consists of deposited droplets and partial deposition part of splashing droplets, see also Stanton and Rutland (1996). Droplets deposit on the wall when the impact energy (i.e. $We_{nb} < 2$) is extremely low. Partial deposition occurs also at higher impact Weber numbers $30 < We_{nb} < 80$, when portions of the spreading droplet lose their kinetic energy due to dissipation. The upper limit of impact Weber number for deposition of a droplet without splashing also depends on the some additional parameters such as surface roughness and average depth of accumulated liquid film on the wall, e.g. splashing takes place faster for rough surfaces as postulated by Mundo et al. (1998). Also it is shown by Cossali et al. (1997) that in the case of a single drop impact onto a stationary liquid film, the number of secondary droplets decreases as the depth of liquid layer is increased. Therefore, the ratio of average wall roughness to the average primary droplet size ($\bar{\varepsilon}^* = \bar{\varepsilon}/d_b$, where $\bar{\varepsilon}$ is the average of roughness of the target surface) should be considered if rough or structured surfaces are used. Also the ratio of the average liquid film

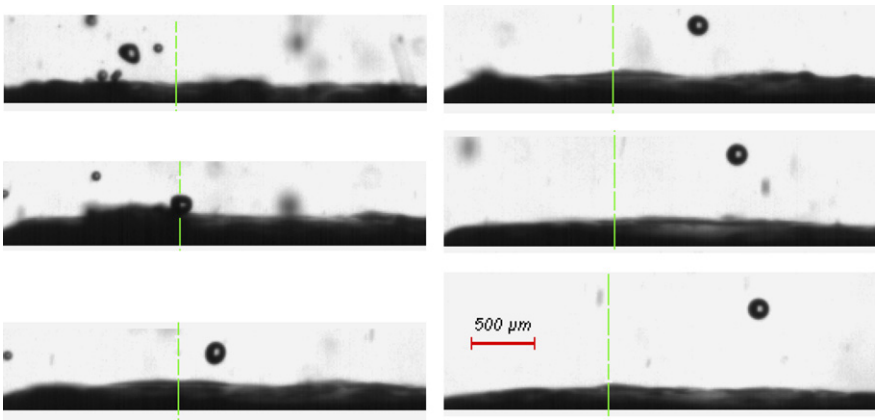

Fig. 6. Exemplary sequence of drop rebound in a spray ($d_b \cong d_a = 172$ µm, $We_{nb} = 10$, time interval between frames is 0.55 ms).

thickness accumulated on the wall to the average primary droplet size ($\bar{h}^* = \bar{h}/d_b$) must be considered in the case of accumulated wall film. For smooth surfaces, the upper limit for deposition-splashing is expressed using a K-factor ($K = Oh \cdot Re^{1.25}$; where Oh is Ohnesorge number defined as: $Oh = \sqrt{We}/Re$ and Re is Reynolds number defined as: $Re = \rho u d/\mu$, where μ is fluid dynamic viscosity). This limiting criterion can be also taken from an Oh–Re diagram, see e.g. Mundo et al. (1997). Other splashing parameters, $K = f(\bar{h}^*)$ have been introduced for thin liquid film conditions, e.g. $K = 2100 + 5880 \cdot \bar{h}^*$, see Cossali et al. (1997). Furthermore it seems that the velocity fluctuations inside the accumulated wall film have an influence on the splashing phenomenon.

In Table 1, four different liquid film regimes are classified based on a threshold Weber number (We_{th}) required for the onset of splashing. The value of Weber number required for the onset of splashing is constant for the case of $\bar{h}^* \leqslant 0.1$ (wetted wall) as proposed by Schmehl et al. (1999). The threshold Weber number then increases monotonically with an increase of the dimensionless film thickness up to $\bar{h}^* = 1$ (thin liquid film) and then decreases until $\sim \bar{h}^* = 2$ (shallow liquid film) and finally takes an asymptotic value corresponding to a deep liquid layer (deep pool condition). The boundary value $\bar{h}^* = 2$ is already considered by Macklin and Metaxas (1976) for shallow–deep liquid film boundary condition. This classification has been postulated based on the measurement data obtained by Wang et al. (2002), for 70% glycerol–water solution.

For the deep film condition (i.e., $\bar{h}^* > 2$), the inertia dominated impacting droplet creates a crater in the liquid film leading to bubble entrainment inside the film and formation of an uprising central jet. This phenomenon is well known and described in the case of a single droplet impact onto a stationary deep liquid layer by Ogüz and Prosperetti (1990) or Fedorchenko and Wang (2004).

Fedorchenko and Wang (2004) have used the dimensionless capillary length ($l_C^* = [2\sigma/(\rho g)]^{1/2}/d_0$) to define two asymptotic conditions describing the central jet phenomenon, as summarized in Table 2. In this Table, R_{max}^*, h_{jet}^*, d_{jet}^* and u_{cj}^* denote respectively the dimensionless maximum cavity radius and height and the diameter and velocity of the uprising central jet created after the cavity recedes. Each parameter is normalized using the drop size or velocity before impact (i.e., $h_{jet}^* = h_{jet}/d_0$ or $u_{cj}^* = u_{cj}/u_0$). In the case of a normal single droplet with a relative small impact velocity, the first condition ($l_C^* \ll 1$) applies, whereas the second condition ($l_C^* \gg 1$) is mostly important for spray impact phenomena. Results presented in Table 2 indicate that gravity docs not play an important role in the formation md dynamics of uprising control jets in the case of $l_C^* \gg 1$. The coefficient c_i in Table 2 is given by Fedorchenko and Wang (2004) as 2.75. In the conducted experiments used in this study, l_C^* varies in the range $80 \leqslant l_C^* \leqslant 180$.

The foregoing survey of literature and phenomenological characterization of spray impact leads us to two fundamental conclusions: Modelling spray impact must consider also the presence and influence of the accumulated wall film; Models based solely on the impact of single droplets will miss many essential elements of

Table 1
Classification of film thickness formed on the wall due to spray impact ($Oh = 0.038$)

Dimensionless film thickness ($\bar{h}^*$)	Wall film condition	Variation of threshold Weber number for onset of splashing	Correlation We_{th}
$\bar{h}^* \leqslant 0.1$	Wetted wall	Constant	~480–500
$1.0 < \bar{h}^* \leqslant 1$	Thin liquid film	Increasing	$1366\bar{h}^* + 354$
$1 < \bar{h}^* \leqslant 2$	Shallow liquid film	Decreasing	$\sim 1657\bar{h}^{*-0.54}$
$\bar{h}^* > 2$	Deep liquid layer	Constant (asymptotic value)	~1100

Table 2
Asymptotic values for characterization of cavity and uprising central jet

Non-dimensional capillary length	$l_C^* \ll 1$	$l_C^* \gg 1$
R_{max}^*	$(Fr/3)^{1/4}$	≈1
h_{jet}^*	$1.43Fr^{1/4}$	≈3/8
d_{jet}^*	$0.57Fr^{1/4}$	≈8/3
u_{cj}^*	$0.913_{c_1} \cdot Fr^{-3/8}$	$1.618_{c_1} \cdot We^{-1/2}$

spray impact. These conclusions are motivation to formulate models derived from spray impact data obtained under controlled boundary conditions; hence also the motivation to perform such experiments.

2. Experimental set-up

The experimental arrangement used in this work is pictured in Fig. 7. The water spray was created using two different hollow cone (pressure swirl) nozzles from Delevan and two different full cone nozzles from Spraying System Co., operated at pressures between 3 and 7 bars. The chosen hollow cone nozzles produce a spray angle of about 70° at a flow rate of 1 or 1.5 l/h. Both flow rate and pressure were variable and measured. The targets were also varied, using the end face of a steel cylinder ($D = 5$ and 15 mm diameter) and a 94 mm diameter steel sphere. This target boundary condition affects the accumulation of the liquid film on the target.

The nozzles were placed at ($X_{\text{nozzle}} = -15$, -20, -30, -40 and -50 mm) above the target and varied in displacement from the target central axis on the target diameter. The coordinate system used for the measurement grid is shown in Fig. 8a.

To characterise the spray a dual-mode phase Doppler instrument from Dantec Dynamics was used, comprising a transmitting optics with a 400 mm focal length, a receiving optics with a 310 mm focal length, an "A" type mask and a 34° scattering angle. By using a dual-mode configuration both normal and tangential velocity components of each individual droplet and its diameter were measured 1 mm above each target

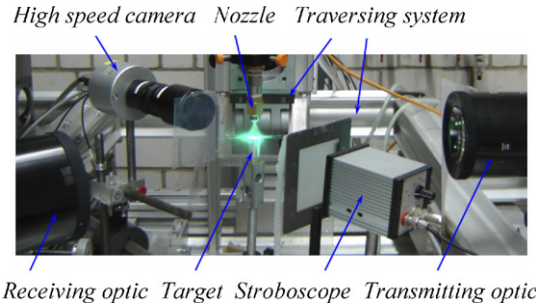

Fig. 7. Photograph of the experimental set-up for spray impact studies, showing the CCD camera and the phase Doppler measurement system.

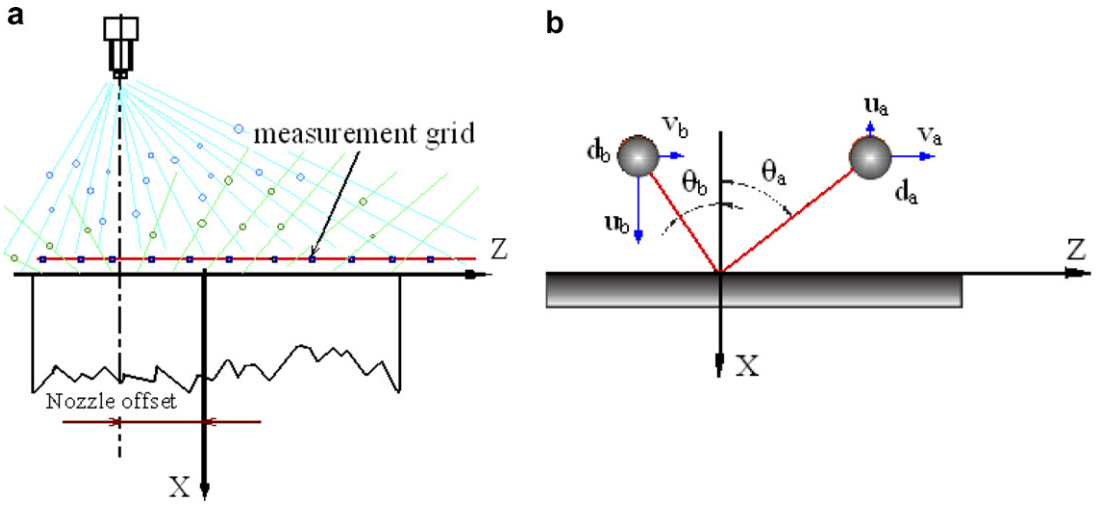

Fig. 8. (a) Coordinate system, and (b) nomenclature for impinging and ejecting droplets.

(i.e., $x = -1$ mm). The ingoing and outgoing droplets are distinguished using the sign of the velocity component normal to the target, i.e. positive u denotes an impacting droplet and a negative u denotes a secondary droplet, see Fig. 8b.

The overall size distributions were corrected for the size dependent detection volume cross-section using the standard system software. In these experimental results, each single point corresponds to averaging 7000–20,000 samples, e.g. d_{10} is defined as: $d_{10} = (\sum_{i=1}^{N} d_i)/N$, where N is number of acquired data at each single measurement point.

The thickness of the liquid film created under spray impact has been estimated based on multiple images obtained by using a Sensicam CCD camera (Fig. 7). Another high-speed camera with 32,000 fps has been used to follow the deposited or ejected droplets from the wall, as shown for two exemplary cases in Figs. 3 and 6.

Surface roughness of the rigid targets has been characterized by means of a mechanical profile meter from Hommelwerke Co., type TK300. Mean roughness (R_a or $\bar{\varepsilon}$) of the target surfaces used in this study ($R_a = \frac{1}{lr}\int_0^{lr} |x(z)|dz$, where lr is the measured length on the target surface) varied in the range $0.2\ \mu m < R_a < 0.67\ \mu m$, whereas mean peak-to-valley roughness (R_z) of the used targets varied in the range $1.3\ \mu m < R_z < 6.6\ \mu m$ ($R_z = \frac{1}{N}\sum_{i=1}^{N} xt_i$, where N is number of the measured points on the target surface), see Fig. 9a and b. In this study, the relative surface roughness in comparison to the mean measured drop size or average accumulated wall film thickness was negligible, see Table 3.

2.1. Effect of target position

Two exemplary single-point measurements of drop diameter count with and without the target are presented in Fig. 10, which illustrate the effect of target position on the probability density distribution of the primary droplet sizes. In the first case, a 5 mm cylindrical target was placed at the centerline of the spray, 20 mm under the nozzle exit (Fig. 10a). In the second case (Fig. 10b) the measurement position is moved 15 mm off-axis. These two measurements differ significantly, indicating clearly the influence of the carrier flow on the measured drop size number density distribution.

The range of measured quantities obtained in the present study is summarized in Table 3.

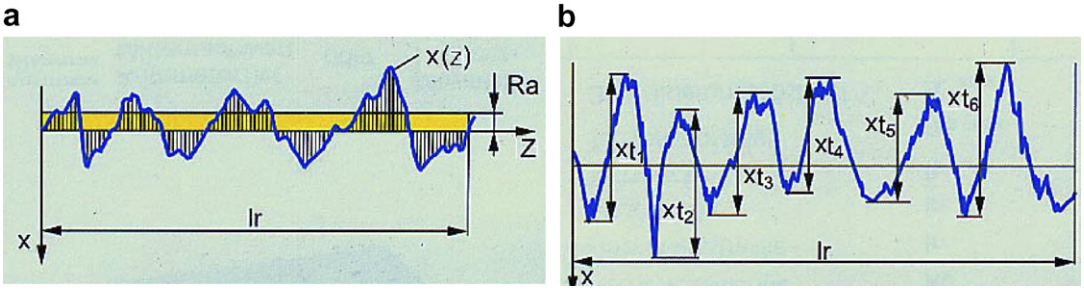

Fig. 9. (a) Mean roughness (R_a or $\bar{\varepsilon}$), and (b) mean peak-to-valley roughness (R_Z) of the target surface.

Table 3
Summary of the measured range of quantities

Measured quantity	Unit (SI)	Before impact	After impact
Droplet size (mean)	μm	21–47	24.5–50
u-velocity	m/s	0.5–15.5	0.5–3.1
v-velocity	m/s	0.05–4.8	0.2–4.15
Weber	–	2–167	6.5–13
Reynolds	–	10–560	12–180
Droplet angle (θ)	(°)	1–70	42–82
Average film thickness ($\bar{h}$)	μm	–	8–107
Mean roughness (R_a)	μm	0.2–0.67	–
Mean peak-to-valley roughness (R_Z)	μm	1.3–6.6	–

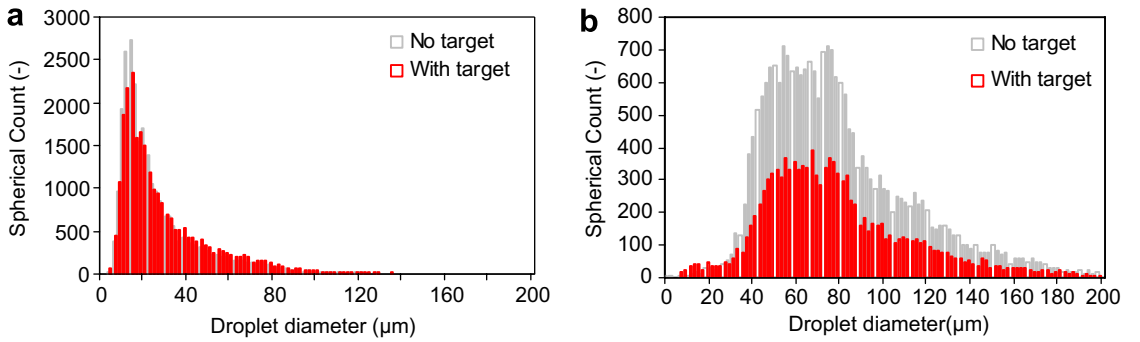

Fig. 10. Two exemplary single-point measurements of primary droplet count with and without target at 20 mm under nozzle exit: (a) on the spray axis: $z = 0$, and (b) off-axis: $z = 15$ mm.

3. Results and discussion

The goal of the present study is to formulate an empirical model of spray impact, taking into account the most influential governing factors, in particular the influence of the liquid film. Measurement data has been considered for a wide range of impact parameters and boundary conditions. Although it is not feasible to present all of the measurement data, the correlations presented will be derived from the entire data set. Therefore in the following sections exemplary measurements of the different spray characterizing quantities will be presented in order to illustrate the origins of the model correlations.

3.1. Distribution of droplet size

Some typical measurement results of drop size distributions are presented in Fig. 11, in which the probability density distributions for the primary and secondary droplet sizes are shown for four measurement points. These points differ significantly in the computed ejected mass fraction, given as λ_m ($\lambda_m = \dot{m}_a/\dot{m}_b$, ejected mass to impinging mass). This particular comparison has been chosen to illustrate that the number density of ejected drops can be higher for a lower mean Weber number of the impacting droplets, but that the ratio $\lambda_{Web} = We_{th}/We_{nb}$ is so very influential, Fig. 11a and b correspond to normal impact conditions ($\lambda_{Web} < 0.1$), whereas Fig. 11c and d illustrate results for oblique impact conditions ($\lambda_{Web} \geqslant 0.1$), as will be discussed in more detail in Section 3.5.

A further result in Fig. 12a shows that the average secondary droplet size (d_{10a}) increases slightly with increasing impact droplet size ($d_{10a} = (\sum_{i=1}^{N} d_{a_i})/N$, where N is number of acquired samples at each single measurement point). The average drop size ratio (secondary to impacting drop size) falls within the fairly narrow range $0.8 < \lambda_{d10} < 1.2$ over all measurement positions and operating conditions as indicated in Fig. 12b. This ratio consistently decreases with increasing Weber number (We_{nb}) based on the normal component of velocity before the impact. A linear correlation can be used to describe this dependency, as

$$\lambda_{d10} = d_{10a}/d_{10b} = -0.003 \cdot We_{nb} + 1.2 \tag{3}$$

where d_{10a} and d_{10b} are the arithmetic mean droplet diameters of ejected droplets and impinging droplets, respectively.

3.2. Distribution of velocity

In Fig. 13 the velocity of ejected droplets is compared with the velocity of the impacting droplets for each of the normal and tangential components for one specific spray condition, albeit very representative of other operational conditions. These velocities are shown as a function of measurement position above the target and for a single position of the nozzle. The results indicate clearly that the normal component of velocity for ejected droplets never exceeds about 3 m/s and this is valid for all experiments conducted in this study,

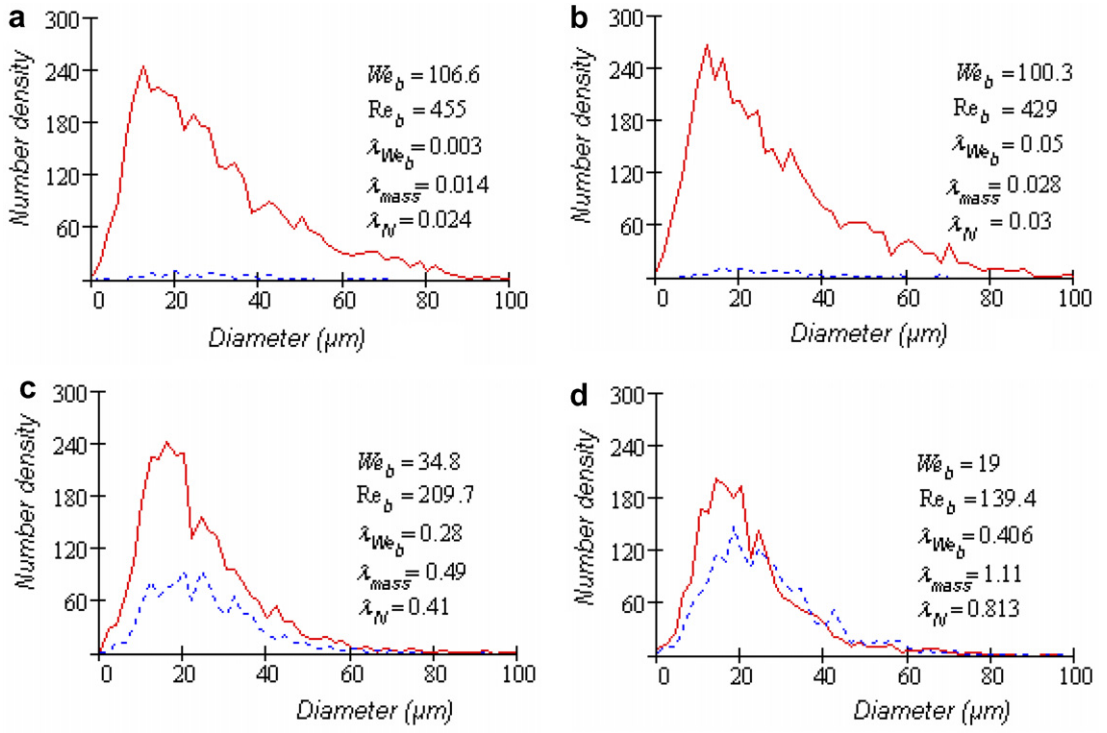

Fig. 11. Probability density distribution of primary and secondary droplet sizes for four measurement points; solid line: before impact, dashed line: after impact.

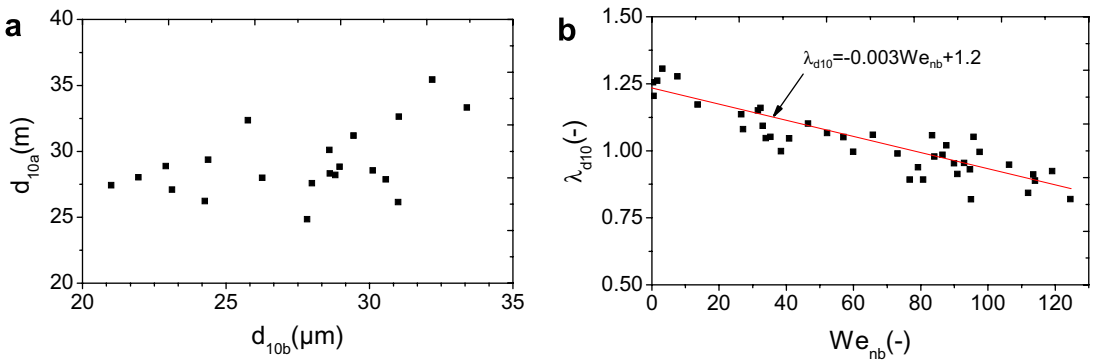

Fig. 12. (a) Correlation between mean drop size before and after impact, and (b) correlation for drop size ratio normal impact Weber number.

despite the fact that the impingement velocity extended beyond 11 m/s. Perhaps even more interesting is that this magnitude is very poorly correlated with the normal component of impingement velocity (Fig. 13a). On the other hand the tangential component of ejection velocity behaves quite differently. Not only does the ejected magnitude sometimes exceed the impingement magnitude (e.g. $0 \lesssim 2z/D \lesssim 0.5$), the two are also very closely correlated with one another. Clearly the tangential momentum is conserved to a large extent upon impingement, whereas the normal momentum is dissipated or diverted into the tangential momentum. Any model describing the spray impingement must reflect such observations.

The results show that the ratio of the normal component of velocity (u_a/u_b) decreases with increasing Weber number (We_{nb}) based on the normal component of velocity before the impact (Fig. 14a), but the ratio of

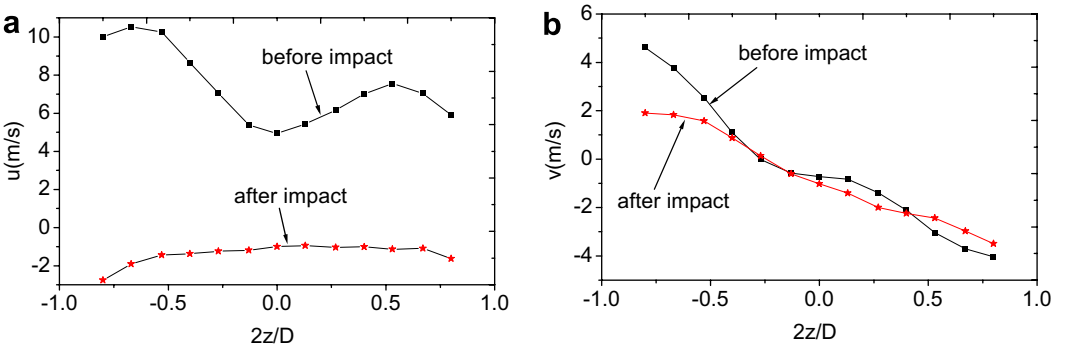

Fig. 13. Comparison of droplet velocity before and after impact for various positions of the measurement volume above the $D = 15$ mm target: (a) normal component, and (b) tangential component; average film thickness $\bar{h} \approx 20$ μm.

tangential component of velocity (v_a/v_b) is independent of the impact Weber number (Fig. 14b). The ratio (u_a/u_b) falls in the range $0.15 < (u_{nb}/u_{na}) < 0.5$ for $We_{nb} > 10$. A general correlation for normal component of velocity can be written as

$$u_a/u_b = -1.1 \cdot (We_{nb})^{-0.36} \tag{4}$$

On the other hand, a linear correlation between the tangential component of velocities before and after impact was found for all measurement conditions as

$$v_a = 0.862 \cdot v_b - 0.094 \tag{5}$$

as illustrated in Fig. 14c.

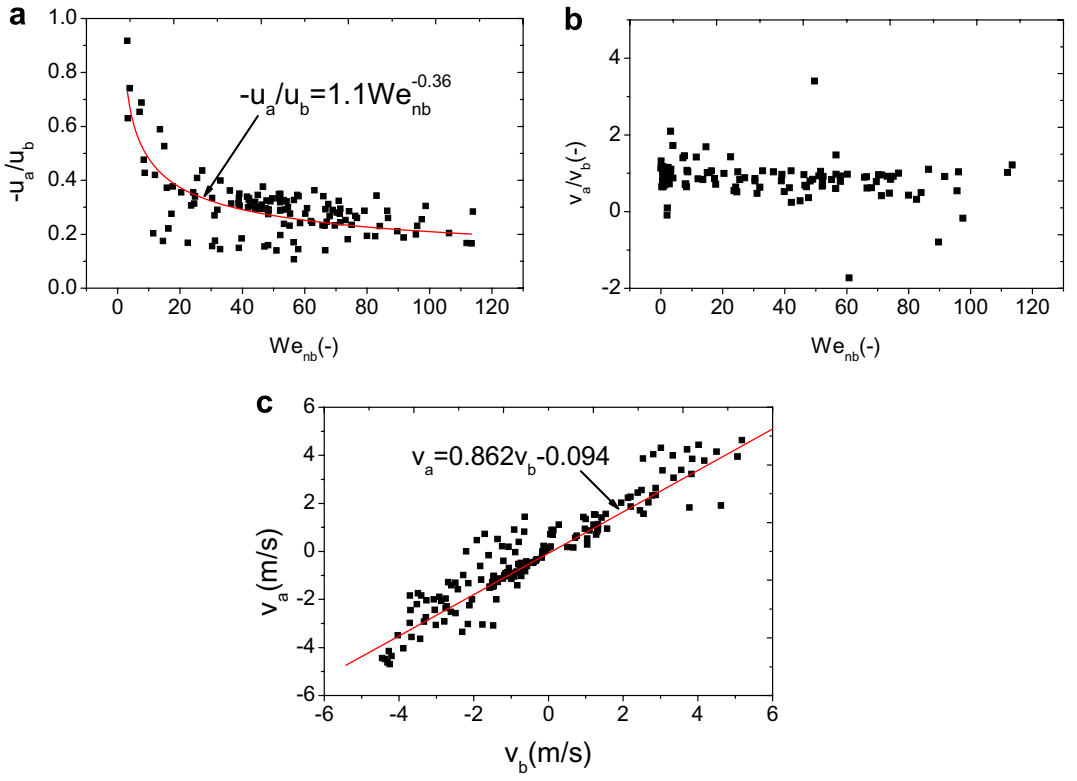

Fig. 14. Mean velocity ratio of ejected to impinging droplets as a function of impact Weber number: (a) normal component, (b) tangential component, and (c) tangential component of after against before impact velocity.

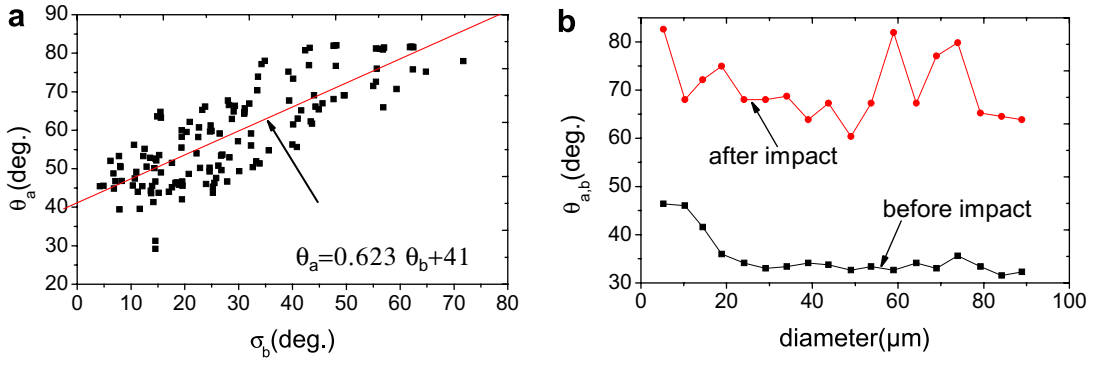

Fig. 15. (a) Correlation between mean ejection angle and impingement angle of droplets, collected over all experiments; (b) impingement (θ_b) and ejection (θ_a) angle of droplets at a single measurement point and as a function of droplet diameter.

3.3. Trajectory of secondary droplets (ejection angle of secondary droplets)

The ejection angle of the droplets depends strongly on the impingement angle, as shown in Fig. 15a, A correlation of these results yields:

$$\theta_a\ [^\circ] = 0.623 \cdot \theta_b\ [^\circ] + 41^\circ \tag{6}$$

The correlation expressed in Eq. (6) indicates that the ejection angle of secondary droplets is on average much higher than that of primary droplets. This is consistent with data presented in Section 3.2 for the normal and tangential velocity components since

$$\theta_a = \tan^{-1}(v_a/u_a) \tag{7}$$

In non-dimensional terms the ejection angle dependence on impact Weber number can be expressed as

$$\eta = \tan\theta_a/\tan\theta_b = 0.784We_{nb}^{0.36} \tag{8}$$

This functional dependence is illustrated in Fig. 16 and shows that the ejection angle of droplets is almost always larger than the impingement angle.

Note, that if any one measurement point is examined in more detail, no significant dependence of ejection angle on droplet diameter can be observed, as exemplary shown in Fig. 15b. Only for very small droplets is a small increase in impingement and ejection angle observed (i.e., $d_b < 20$ μm).

3.4. Distribution of the ejection Weber number

The previous results can also be examined in terms of Weber number before and after the impact, in this case computed using the velocity magnitude. Such a diagram is shown in Fig. 17, in which the Weber number

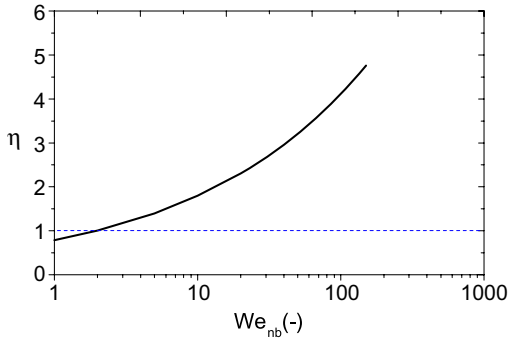

Fig. 16. Coefficient of ejection angle of secondary droplets.

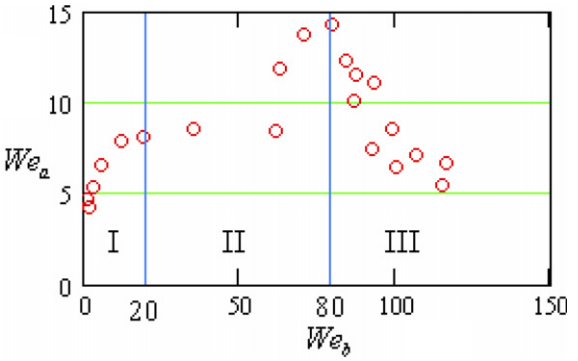

Fig. 17. Weber number of ejected droplets against impact Weber number.

of ejected droplets first increases with increasing impact Weber number, but then after reaching a maximum value, again decreases. In this representation three regimes can be identified: first a low impact Weber number range ($We_{nb} < 20$) in which the rebounded droplet increases with increasing the Weber number (region I in Fig. 17). This is followed by deposition range ($20 < We_{nb} < 80$), in which the deposition rate is high and fewer secondary drops are ejected (region II in Fig. 17), and finally at high Weber numbers $We_{nb} > 80$. a condition of splashing or ejected wall film, in which the secondary droplets ejected from splashed corona are small and also the velocities are small, leading to lower ejection Weber numbers (region III in Fig. 17). The Weber number 80 is often found in the literature as a limit for splash onset, see e.g., Bai and Gosman (1995).

At any single measurement point, the impact Weber number increases linearly with mean droplet diameter, whereas the ejected Weber number at first increases with diameter (up to $d_b \approx 20$ μm) then does not change significantly or decreases, as illustrated in Fig. 18a and b.

3.5. Distribution of secondary to incident mass and number ratios

The total secondary-to-incident mass ratio ($\lambda_m = \dot{m}_a/\dot{m}_b$) is affected by several complex parameters such as droplet Weber number based on the normal component of impact velocity (We_{nb}), impact Weber number ratio (We_{tb}/We_{nb}), impact Reynolds number (Re_{nb}; where $Re_{nb} = \rho u_b d_{10b}/\mu$), relative wall roughness ($\bar{\varepsilon}^* = \bar{\varepsilon}/d_b$) aid relative wall film thickness ($\bar{h}^* = \bar{h}/d_b$); hence a general correlation for mass ratio is difficult to derive. Generally, the overall secondary-to-incident mass ratio ($\lambda_m = \dot{m}_a/\dot{m}_b$) at any one point can be expressed in dimensionless form as

$$\lambda_m = (\dot{m}_a/\dot{m}_b) = f\left(We_{nb}, \lambda_{We_b}, Re_b, \bar{\varepsilon}^*, \bar{h}^*\right) \tag{9}$$

Based on previous experimental observations reported by Bai and Gosman (1995), λ_m takes a random value in the range $[0.2, 0.8]$ for spray impact onto a dry wall and $[0.2, 1.1]$ for spray impact onto a wetted wall.

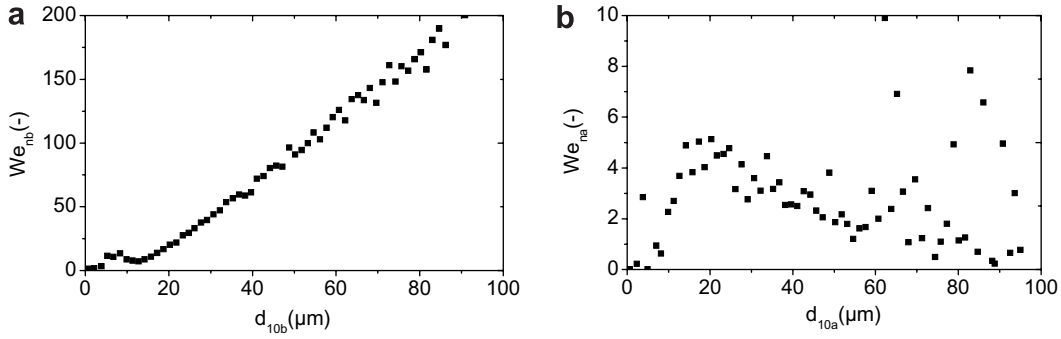

Fig. 18. Distribution of: (a) impact, and (b) ejection Weber numbers at a single measurement point above a spherical target.

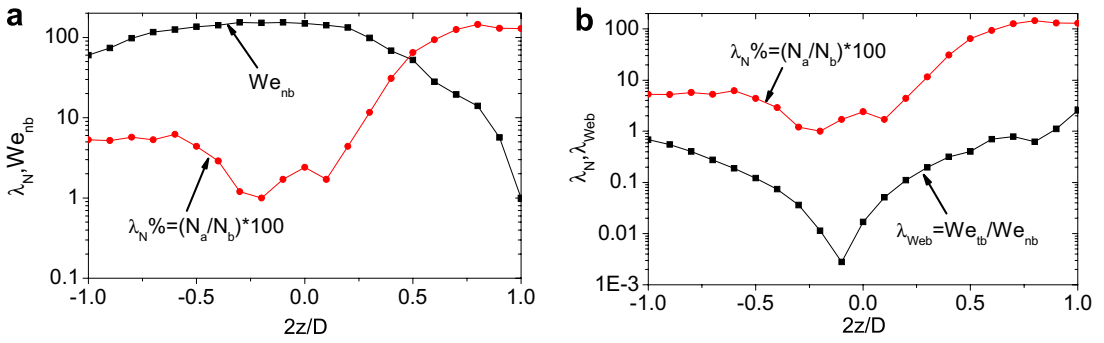

Fig. 19. (a) Variation of number and Weber number ratio across the target: (a) number ratio (λ_m) and Weber number based on the normal velocity component before impact (We_{nb}), and (b) number ratio (λ_N) and Weber number ratio $\lambda_{We_b} = We_{tb}/We_{nb}$.

The result of the present study indicates that the Weber number ratio, We_{tb}/We_{nb}, which compares the ratio of the square of the tangential velocity to the normal velocity before impact, plays an important role in the spray–wall interaction phenomena, see also Kalantari and Tropea (2005). As an example, the mass and number ratios ($\lambda_m = \dot{m}_a/\dot{m}_b$, $\lambda_N = N_a/N_b$) correlate with this Weber number ratio better than with the normal component of impact velocity in the Weber number (We_{nb}), at least for the oblique impact condition and relatively constant film thickness. To illustrate this, λ_N is plotted together with We_{nb} (Fig. 19a), and with $\lambda_{We_b} = We_{tb}/We_{nb}$ (Fig. 19b) for the same data set across the impact target ($D = 15$ mm). The impact obliqueness changes in the approximate range $0° < \theta < 26°$ over the z-positions shown in Fig. 19a and b. It can be seen that in the latter case that the two quantities exhibit a very similar behaviour, indicating a strong correlation. This result indicates clearly that the spray–wall interaction models based on the results from normal drop impact alone cannot adequately describe the actual conditions of spray impact phenomena. The quantity λ_m behaves similarly.

Generally, in an oblique impact condition the secondary-to-incident mass ratio (λ_m) decreases with the impact Weber number based on the normal component of velocity (We_{nb}), but increases with the impact Weber number ratio (λ_{We_b}). In the case of a normal impact condition, the quantity λ_m increases with the impact Weber number based on the normal velocity component. Therefore two different impact conditions can be defined as:

- Normal impact: $\lambda_{We_b} = We_{tb}/We_{nb} < 0.1$, for which no significant dependency between secondary-to-incident mass ratio (λ_m) and impact Weber number ratio (λ_{We_b}) was observed, Fig. 20a.
- Oblique impact: $\lambda_{We_b} = We_{tb}/We_{nb} \geqslant 0.1$, for which the secondary-to-incident mass ratio (λ_m) increases with impact Weber number ratio (λ_{We_b}), Fig. 20b.

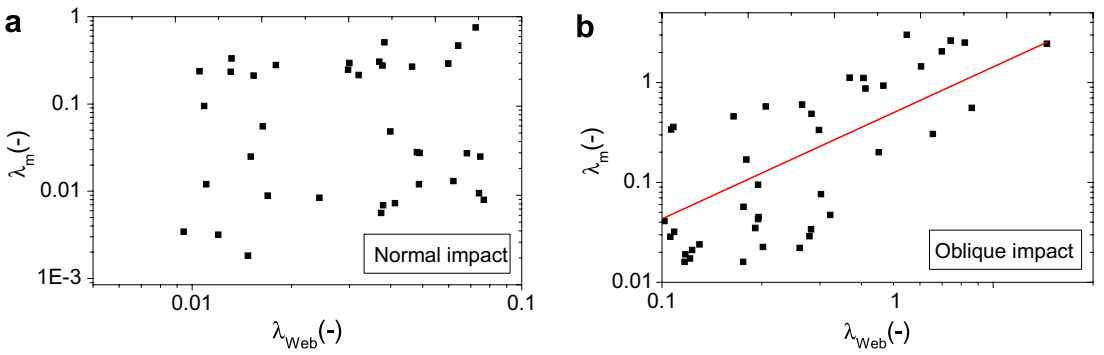

Fig. 20. Distribution of secondary-to-incident mass ratio (λ_m) for: (a) normal impact condition $\lambda_{We_b} < 0.1$, and (b) oblique impact condition $\lambda_{We_b} \geqslant 0.1$.

In the case of normal impact ($\lambda_{We_b} < 0.1$), the secondary-to-incident mass ratio (λ_m) mostly falls in the range [0.002, 0.85], whereas this ratio falls in the range [0.016, 1.12] for oblique impact conditions ($\lambda_{We_b} \geqslant 0.1$). The upper limit of the mass ratio in the case of oblique impact (i.e., $\lambda_m = 1.12$) clearly indicates that for some conditions more liquid mass is ejected from the wall film than impacts with the drops, at a given measurement point on the target surface.

For all of the conducted measurements, the two limiting values, $\lambda_m > 1$ and $\lambda_m < 0.01$ were observed for oblique and normal impact conditions, respectively, see Fig. 20a and b.

The results of this study indicate that in the case of normal impact conditions ($\lambda_{We_b} < 0.1$), the secondary-to-incident mass and number ratio, λ_m and λ_N, increase linearly with the impact Weber number based on the normal component of the impact velocity (We_{nb})

$$\lambda_m = (\dot{m}_a/\dot{m}_b) = 6.74 \times 10^{-3} \cdot We_{nb} - 0.204 \tag{10}$$

$$\lambda_N = (\dot{N}_a/\dot{N}_b) = 2.16 \times 10^{-3} \cdot We_{nb} + 8.96 \times 10^{-2} \tag{11}$$

These correlations were derived using all conducted measurements in the range $35 \leqslant We_{nb} \leqslant 165$ and $\lambda_{We_b} < 0.08$, Fig. 21a and b.

In the case of oblique impact condition ($\lambda_{We_b} > 0.1$), the secondary-to-incident mass and number ratio (λ_m, λ_N) behave quite differently. These two quantities λ_m and λ_N decrease with the impact Weber number based on the normal component of the impact velocity (We_{nb}) and increase with the impact Weber number ratio (λ_{We_b}), see Figs. 20b and 22a and b. In contrast to the results presented in Fig. 21a and b for normal impact condition, larger secondary-to-incident mass and number ratios can be observed for smaller impact Weber

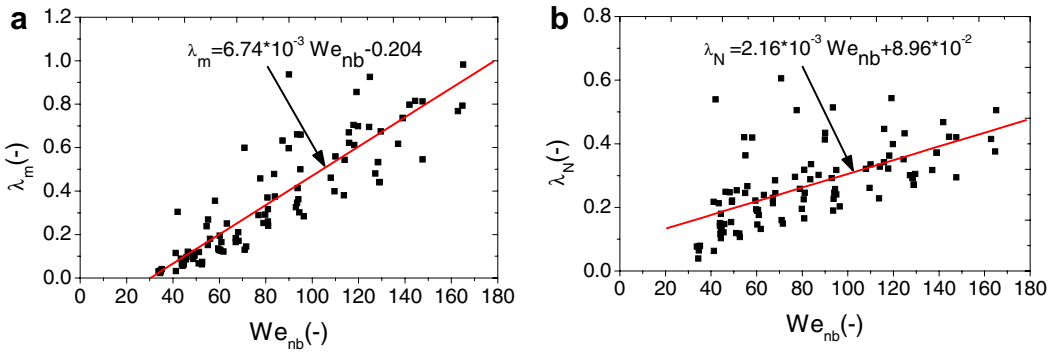

Fig. 21. Correlation of secondary-to-incident: (a) mass ratio λ_m, and (b) number ratio λ_N with impact Weber number based on the normal component of velocity We_{nb} for normal impact conditions $\lambda_{We_b} < 0.1$.

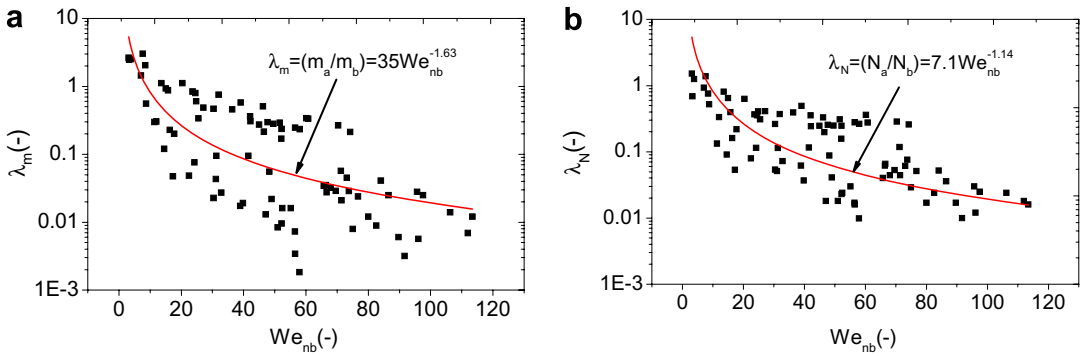

Fig. 22. (a) Correlation of secondary-to-incident: mass ratio λ_m and number ratio λ_N and (b) with impact Weber number based on the normal component of velocity We_{nb} for oblique impact condition $\lambda_{We_b} > 0.1$.

numbers in the case of an oblique impact condition, as illustrated in Fig. 22a and b. This is due to a larger impact Weber number ratio (λ_{We_b}) at smaller impact Weber numbers (We_{nb}) for oblique impact conditions, see also Fig. 20b. Note that in the case of oblique impact conditions, the impact Weber number ratio simultaneously increases with decreasing impact Weber number based on the normal component of impact velocity.

In summary, a dilemma in modelling arises, since for oblique impact the outcome depends on both We_{nb} and λ_{We_b}. To capture both dependencies would require a much deeper insight into the physics involved and probably much more data, whereby it is not at all clear that the reliability of the resulting correlations would improve. In the present work both possibly correlations have been examined and the most favourable are expressed in terms of We_{nb} as:

$$\lambda_m = (\dot{m}_a/\dot{m}_b) = 35 \cdot We_{nb}^{-1.63} \tag{12}$$

$$\lambda_N = (\dot{N}_a/\dot{N}_b) = 7.1 \cdot We_{nb}^{-1.14} \tag{13}$$

These expressions were derived using all conducted measurements in the range $10 < We_b < 160$ and $0.1 < \lambda_{We_b} < 0.86$ which are pictured in Fig. 22a and b. These expressions are valid for smooth target surfaces, i.e., $\bar{\varepsilon}^* = \bar{\varepsilon}/d_b \ll 1$. The average thickness of accumulated wall film for these measurements is described in the following section.

3.6. Average film thickness

Parallel to the drop measurements using the phase Doppler technique, visualization of the liquid film on the target was performed in order to estimate the average thickness of the liquid film. Such visualization and its evaluation are pictured in Fig. 23. The average film thickness was then calculated by averaging several instantaneous film thicknesses obtained by the high-speed CCD camera. In the experiments reported above, the mean film thickness varied in the range $8\ \mu m \leqslant \bar{h} \leqslant 107\ \mu m$ for corresponding impingement Weber numbers in the range $10 < We_{nb} < 160$.

The average film thickness depends on the several parameters of impacting spray; normal and tangential component of impact velocity u_b and v_b, flux density of impacting spray ($\dot{q} = q/A$; "q" and "A" to be flux of the impacting spray and the reference area over which flux is measured), volume-averaged diameter of impacting droplets (d_{30b}), dynamic viscosity of the liquid used in spray (μ) and also the boundary condition of the target; average target surface roughness ($\bar{\varepsilon}^*$) and target size (D) and shape. A general expression for the average film thickness can be written as

$$\bar{h} = \psi\left(u, v, d_{30b}, \dot{q}, \mu, \bar{\varepsilon}^*, D_{spray}/D\right) \tag{14}$$

where, D_{spray} is the diameter of the effective impinging spray on the target defined as: $D_{spray} = 2x_{Nozzle} \cdot \tan(\alpha/2)$, α is the spray cone angle. The parameters u, v, d_{30b}, $\dot{q}$ and D_{spray} vary with nozzle pressure and nozzle height

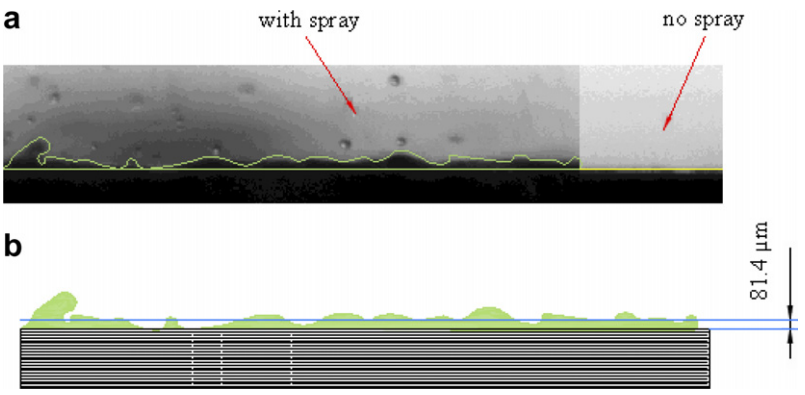

Fig. 23. Thin liquid film formed under spray impact: (a) original image of CCD camera with interface contour added, and (b) synthesized image to be integrated yielding the average film thickness.

above the target. The three first parameters may be combined into an impact Weber number. The volume averaged droplet diameter, d_{30b}, is defined as:

$$d_{30b} = 3\sqrt{\frac{1}{N}\sum_{i=1}^{N} d_{b_i}^3} \tag{15}$$

Results of this study indicate that the average film thickness decreases with increasing the nozzle pressure at a given nozzle height, Fig. 24a. In Fig. 24b the variation of the measured average film thickness ($\bar{h}$) as a function of impact Reynolds number based on the normal component of velocity is presented for a relative negligible surface roughness and a normal impact condition, i.e., the impact Weber ratio was negligible ($\lambda_{We_b} \leqslant 0.023$). It is shown in Fig. 24b that the average film thickness decreases significantly with the impact Reynolds number in this experiment. A simple correlation for variation of the average film thickness as a function of impact Reynolds number can be expressed as

$$\bar{h}/d_{30b} = a \cdot Re_{nb}^{-b} \tag{16}$$

The coefficients a and b were found to be 22149 and 1.769, respectively, based on the measured data in this study for a stainless steel target with 5 mm in diameter ($D = 5$ mm), negligible surface roughness ($\bar{\varepsilon}^* \ll 1$ and $\bar{\varepsilon}^* \ll \bar{h}^*$) and normal impact condition ($\lambda_{We_b} \leqslant 0.023$), see also Kalantari and Tropea (2006).

Two exemplary results of the average film thickness ($\bar{h}$) together with the impact Weber number (We_{nb}), mass ratio (λ_m) and flux density ($\dot{q}$) are illustrated in Fig. 25a and b as a function of nozzle height (x) for two different nozzle pressures (3 and 6 bar) for a stainless steel target with diameter of 5 mm ($D = 5$ mm).

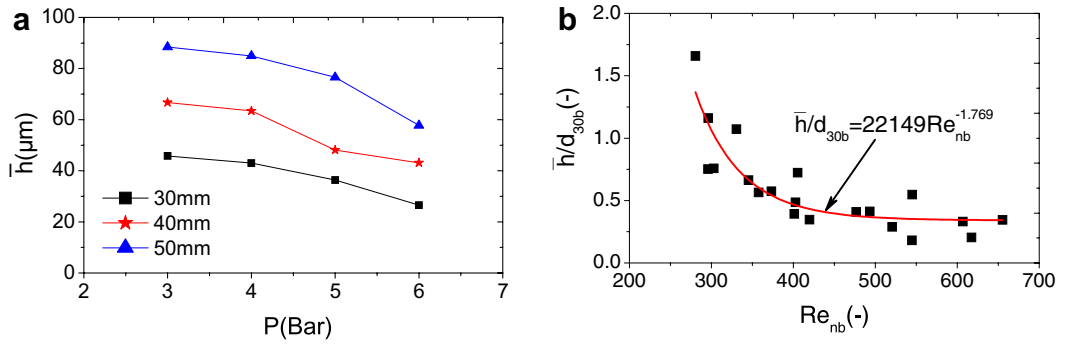

Fig. 24. Variation of the average film thickness: (a) with the nozzle pressure at different nozzle height, and (b) with the impact Re-number, for a stainless steel target with diameter of 5 mm ($D = 5$ mm).

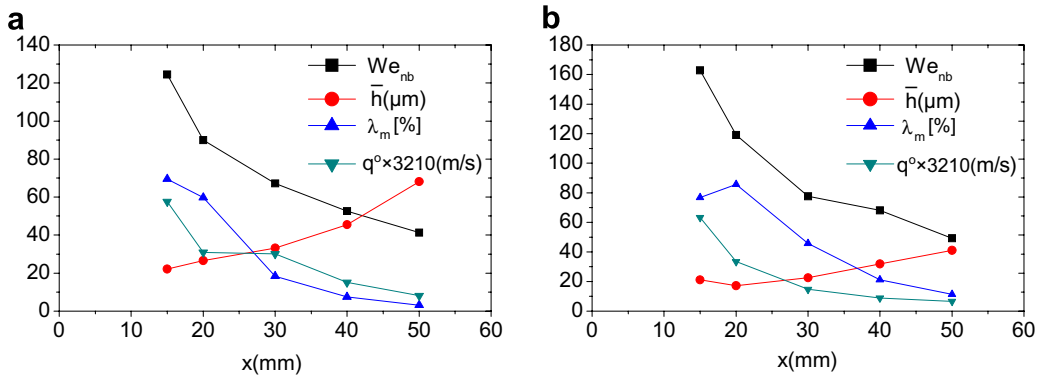

Fig. 25. Variation of the impact Weber number (We_{nb}), average film thickness ($\bar{h}$), mass ratio (λ_m) and flux density ($\dot{q}$) with the nozzle height (x) for two exemplary nozzle pressures: (a) 3 bar, and (b) 6 bar; for a stainless steel target with diameter of 5 mm ($D = 5$ mm).

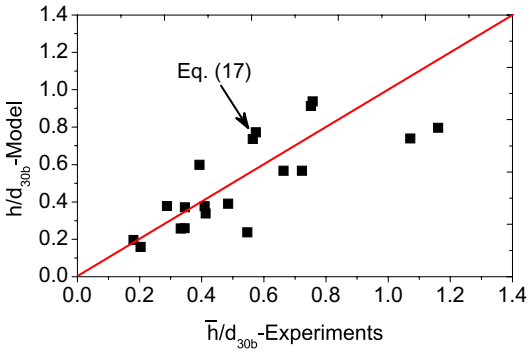

Fig. 26. Prediction of the dimensional analysis (16) for accumulated wall film thickness; each individual average film thickness ($\bar{h}$) is normalized by the volume averaged droplet diameter before the impact (d_{30b}).

It should be noted that both impact Weber number and flux density of impacting drops decrease with the nozzle height. It is shown in this figure that decreasing the impact Weber number yields an increase the accumulated wall film thickness but decrease of the secondary-to-incident mass ratio (λ_m). The same behaviour was observed for the secondary-to-incident number ratio (λ_N). Note that in the conducted experiments, the entire target surface was exposed to the impacting spray, i.e., $D_{spray}/D > 1$.

In the case of an inertial spray impact, i.e. $We/\sqrt{Re} \gg 1$ (see also Pasandideh-Fard et al., 1996) and using the dimensional analysis equation (14) for characterizing the average film thickness accumulated on the wall due to spray impact, the following find expression can be derived:

$$\bar{h} = \xi \cdot d_{30b} \cdot Re_b^{-1/2} \cdot \left(\frac{\dot{q}}{\bar{u}_b}\right)^{\gamma} \tag{17}$$

where ξ and γ are constant values found to be 4 and -0.5, respectively. These constants have been found based on the measured data in this study for normal impact condition ($\lambda_{We_b} \leqslant 0.023$), see also Kalantari and Tropea (2006).

The prediction capability of the dimensional analysis Eq. (17) is presented in Fig. 26. In this figure each individual average film thickness ($\bar{h}$) is normalized by the volume averaged droplet diameter before the impact (d_{30b}). The results presented in this figure indicate good prediction of the average film thickness obtained from dimensional analysis.

4. Conclusions

From these experiments some general conclusions and quantitative experiments about the mean statistics of ejected drop properties as a function of impinging spray properties can be obtained. The quantitative experiments are summarized in Table 4, which are valid for the following experimental conditions:

- Smooth target surface, i.e., negligible surface roughness ($\bar{\varepsilon}^* \ll 1$ and $\bar{\varepsilon}^* \ll \bar{h}^*$).
- The entire target surface exposed to the impacting spray, i.e., $D_{spray}/D > 1$.
- The accumulated wall film thickness in the range 8 μm $\leqslant \bar{h} \leqslant$ 107 μm.
- Impingement Weber number in the range $10 < We_{nb} < 160$, based on the normal component of velocity before the impact.
- Fluids with low viscosity, i.e., $Oh \ll 0.1$.

Some of the more important general observations are given in the points below.

- The average drop size ratio λ_{d10} (ejection to impingement) decreases with increasing Weber number based on the normal component of velocity before the impact (We_{nb}).

Table 4
Summary of the empirical model for spray impact onto flat and rigid walls

Parameter	General correlation	Coefficients	Correlation coefficient
Normal component of velocity (m/s)	$u_a/u_b = -\alpha \cdot (We_{nb})^{-\beta_1}$	$\alpha_1 = 1.1$ $\beta_1 = 0.36$	0.65
Tangential component of velocity (m/s)	$v_a = \alpha_2 \cdot v_b + \beta_2$	$\alpha_2 = 0.862$ $\beta_2 = 0.094$	0.93
Droplet trajectory angle (deg)	$\theta_a = \alpha_3 \cdot \theta_b + \beta_3$	$\alpha_3 = 0.623$ $\beta_3 = 41$	0.80
Mean droplet size (μm)	$d_{10a}/d_{10b} = -\alpha_4 \cdot We_{nb} + \beta_4$	$\alpha_4 = 0.003$ $\beta_4 = 1.2$	0.90
Mass ratio (normal impact, $\lambda_{We_b} < 0.1$)	$\lambda_m = (m_a/m_b) = \alpha_5 \cdot We_{nb} + \beta_5$	$\alpha_5 = 6.74 \times 10^{-3}$ $\beta_5 = -0.204$	0.89
Mass ratio (oblique impact, $\lambda_{We_b} \geqslant 0.1$)	$\lambda_m = \alpha_6 \cdot We_{nb}^{-\beta_6}$	$\alpha_6 = 35$, $\beta_6 = 1.63$	0.72
Number ratio (normal impact, $\lambda_{We_b} < 0.1$)	$\lambda_N = (m_a/m_b) = \alpha_7 \cdot We_{nb} + \beta_7$	$\alpha_7 = 2.2 \times 10^{-3}$ $\beta_7 = 8.96 \times 10^{-2}$	0.64
Number ratio (oblique impact, $\lambda_{We_b} \geqslant 0.1$)	$\lambda_N = (N_a/N_b) = \alpha_8 \cdot We_{nb}^{-\beta_8}$	$\alpha_8 = 7.1$ $\beta_1 = 1.14$	0.70
Average accumulated wall film thickness ($\bar{h}$)	$\bar{h} = \alpha \cdot d_{30b} \cdot Re_b^{-1/2} \cdot \left(\frac{\dot{q}}{\dot{m}_b}\right)^{\gamma}$	$\xi = 4$ $\gamma = -0.5$	–

- The normal component of velocity after the impact does not correlate well with the normal velocity component of the impinging droplet, while the tangential component of the ejected droplets correlates closely with the impingement tangential velocity.
- With increasing impact Weber number the ejection Weber number at first increases and then after reaching a maximum value decreases.
- At each measurement point, the impact Weber number increases monotonically with impact droplet size, while the ejection Weber number at first increases with ejected droplet size and then takes on a relative constant value.
- The mean reflection angle of ejected droplets strongly depends on the mean incident angle of impinging droplet, although no significant relationship between angle of droplets and droplet diameter can be observed at any one single measurement point.
- The mean impact Weber number ratio ($\lambda_{Web} = We_{tb}/We_{nb}$) positively influences the number density of secondary droplets in the case of a oblique impact condition.
- The mass and number ratios ($\lambda_m = \dot{m}_a/\dot{m}_b, \lambda_N = \dot{N}_a/\dot{N}_b$) exhibit a similar behavior compared with the Weber number ratio (λ_{We_b}) for oblique impact conditions ($\lambda_{We_b} > 0.1$). This is not true when these ratios are compared with the normal component of the impingement Weber number (We_{nb}).
- Two different impact conditions can be distinguished in a spray impact onto a flat and rigid wall: (1) normal impact: $\lambda_{We_b} = We_{tb}/We_{nb} < 0.1$, with no significant dependency between secondary to incident mass ratio (λ_m) and impact Weber number ratio (λ_{We_b}) and (2) oblique impact: $\lambda_{We_b} = We_{tb}/We_{nb} \geqslant 0.1$, with secondary to incident mass ratio (λ_m) increasing with impact Weber number ratio (λ_{We_b}).
- In the case of normal impact conditions ($\lambda_{We_b} < 0.1$), the secondary to incident mass ratio (λ_m) increases with impact Weber number based on the normal velocity component (We_{nb}) whereas this ratio decreases with impact Weber number in the case of oblique impact conditions ($\lambda_{We_b} \geqslant 0.1$).
- In the case of normal impact conditions ($\lambda_{We_b} < 0.1$), the secondary to incident mass ratio (λ_m) mostly falls in the range $[0.002, 0.85]$, whereas this ratio falls in the range $[0.016, 1.12]$ for oblique impact conditions ($\lambda_{We_b} \geqslant 0.1$).

- Non-dimensional crown radius and height of a splashing droplet in spray impact phenomena have mostly smaller growth rate in compare with a single or train of drop impact onto a stationary liquid film.
- The average film thickness decreases with increasing the impact Weber number (We_{nb}) in the case of a normal impact condition.

Acknowledgments

D. Kalantari would like to thank the ministry of science and technology of I. R. Iran and University of Mazandaran for financial support of his study in Germany through the scholarship No. 780274.

References

Bai, C., Gosman, A.D., 1995. Development of methodology for spray impingement simulation. Society Automot. Eng. 950283, 69–87.
Bai, C.H., Rusche, H., Gosman, A.D., 2002. Modeling of gasoline spray impingement, Atom. Sprays 12, 1–27.
Ching, B., Golay, M.W., Johnson, T.J., 1984. Droplet impacts upon liquid surfaces. Science 226, 535–537.
Coghe, A., Brunello, G., Cossali, G.E., Marengo, M., 1999. Single drop splash on thin film: measurements of crown characteristics. ILASS-Europe 99, Toulouse, July 5–7th.
Cossali, G.E., Coghe, A., Marengo, M., 1997. The impact of a single drop on a wetted surface. Exp. Fluids 22, 463–472.
Cossali, G.E., Brunello, G., Coghe, A., Marengo, M., 1999. Impact of a single drop on a liquid film: experimental analysis and comparison with empirical models. Italian Congress of Thermofluid Dynamics UIT, Ferrara, 30 June–2 July.
Fedorchenko, A.I., Wang, A.B., 2004. On some common feature of drop impact on liquid surfaces. Phys. Fluids 16, 1349–1365.
Kalantari, D., Tropea, C., 2006. Spray impact onto rigid walls: formation of the liquid film. ICLASS06, Aug. 27–Sep. 01. Kyoto, Japan.
Kalantari, D., Tropea, C., 2005. Experimental study of spray impact onto rigid walls. 20th ILASS-Europe, Orleans, Sept. 5–7th.
Lee, M.M., Hanratty, T.J., 1988. The inhabitation of droplet deposition by the presence of a liquid film. Int. J. Multiphase Flow 14, 129–140.
Macklin, W.C., Metaxas, G.J., 1976. Splashing of drops on liquid layers. J. Appl. Phys. 47, 3963–3970.
Mundo, C., Tropea, C., Sommerfeld, M., 1997. Numerical and Experimental Investigation of Spray Characteristics in the Vicinity of a Rigid Wall. Elsevier, pp. 228–237.
Mundo, C., Sommerfeld, M., Tropea, C., 1998. On the modeling of liquid sprays impinging on surfaces, Atom. Sprays 8, 625–652.
Ogüz, H.N., Prosperetti, A., 1990. Bubble entrainment by the impact of drops on liquid surfaces, I. J. Fluid Mech. 219, 143–179.
Pasandideh-Fard, M., Qiao, M., Chandra, Y.M., Mostaghimi, M., 1996. Capillary effects during droplet impact on a solid surface. Phys. Fluids 8, 650–659.
Roisman, I.V., Tropea, C., 2004. Structure of an impinging spray. In: 4th Int. Symp. Meas. Techn. for Multiphase Flows, Sept. 10–12, Hangzhou, China.
Roisman, I.V., Tropea, C., 2005. Fluctuating flow and jetting in a liquid layer created by an impacting spray. Int. J. Multiphase Flow 31, 179–200.
Roisman, I.V., Prunet-Foch, B., Tropea, C., Vignes-Adler, M., 2002. Multiple drop impact onto a dry solid substrate. J. Colloid Interface Sci. 256, 396–410.
Roisman, I.V., Horvat, K., Tropea, C., 2006. Spray impact: rim transverse instability initiating fingering and splash, and description of a secondary spray. Phys. Fluids 18, 102104.
Schmehl, R., Rosskamp, H., Willman, M., Wittig, S., 1999. CFD analysis of spray propagation and evaporation including wall film formation and spray/film. Int. J. Heat Fluid Flow 20, 520–529.
Sikalo, S., Tropea, C., Ganic, E.N., 2005. Impact of droplets onto inclined surfaces. J. Colloid Interface Sci. 286, 661–669.
Sivakumar, S., Tropea, C., 2002. Splashing impact of a spray onto a liquid film. Phys. Fluids Lett. 14, L85–L88.
Stanton, D.W., Rutland, C., 1996. Modeling fuel film formation and wall interaction in Diesel Engines. SAE paper 960628.
Stanton, D.V., Rutland, C.J., 1998. Multi-dimensional modeling of thin liquid films and spray–wall interactions resulting from impinging sprays. Int. J. Heat Mass. Transfer 41, 3037–3054.
Wang, M., Watkins, A.P., 1993. Numerical modelling of Diesel spray impaction phenomena. Int. J. Heat Fluid Flow 14, 301–311.
Wang, A.B., Chen, C.C., Hwang, W.C., 2002. On some new aspects of splashing impact of drop-liquid surface interactions. In: Rein, M. (Ed.), Drop–Surface Interactions. Springer Alert Pub.-Co.
Yarin, A.L., Weiss, D.A., 1995. Impact of drops on solid surfaces: self-similar capillary waves, and splashing as a new type of kinematics discontinuity. J. Fluid Mech. 238, 141–173.